

# Fermionization of a bosonic gas under highly-elongated confinement: A diffusion quantum Monte Carlo study

D. Blume

*Department of Physics, Washington State University, Pullman, Washington 99164-2814, USA*

(November 1, 2018)

The diffusion quantum Monte Carlo technique is used to solve the many-body Schrödinger equation fully quantum mechanically and nonperturbatively for bosonic atomic gases in cigar-shaped confining potentials. By varying the aspect ratio of the confining potential from 1 (spherical trap) to 10000 (highly elongated trap), we characterize the transition from the three-dimensional regime to the (quasi-)one-dimensional regime. Our results confirm that the bosonic gas undergoes “fermionization” for large aspect ratios. Importantly, many-body correlations are included explicitly in our approach.

## I. INTRODUCTION

One-dimensional systems of impenetrable bosons are predicted to show intriguing behavior, namely *fermionization*. An impenetrable one-dimensional gas of  $N$  bosonic atoms behaves as if the system consisted of  $N$  one-dimensional fictitious spin-less non-interacting fermions, a so-called Tonks or Tonks-Girardeau gas [1–13]. Fermionization has profound effects on the characteristics of a system. The ground state energy of  $N$  non-interacting bosonic atoms in a one-dimensional harmonic trap with trapping frequency  $\nu_z$  is  $E_0^{B,z} = Nh\nu_z/2$ . For comparison, the ground state energy of  $N$  non-interacting spin-less fermionic atoms under the same confinement is  $E_0^{F,z} = N^2h\nu_z/2$ , or  $E_0^{F,z} = NE_0^{B,z}$ . In this paper we map out the transition of a bosonic gas from three- to one-dimensional, and monitor the signatures of fermionization [8,10,13].

A Tonks gas has not been observed experimentally yet, and it is an open question how one would probe a Tonks gas once it has been created. Effectively one-dimensional atomic gases may be realized by confining  $N$  atoms in highly elongated cigar-shaped traps where the two tight confining directions are characterized by the frequency  $\nu_\rho$ , and the weak confining direction by  $\nu_z$ . Correspondingly, the system exhibits two characteristic length scales, the oscillator length in the  $\rho$  direction,  $a_\rho = \sqrt{\hbar/(m\omega_\rho)}$ , and the oscillator length in the  $z$  direction,  $a_z = \sqrt{\hbar/(m\omega_z)}$ , where  $\rho = \sqrt{x^2 + y^2}$ ,  $\omega_{\rho,z} = 2\pi\nu_{\rho,z}$ , and  $m$  the atomic mass of the trapped gas. Such a confining potential has been realized experimentally by Görlitz *et al.* with aspect ratios  $L = \nu_\rho/\nu_z$  as large as 100 [14] (see also [15–17]). These experiments enter the quasi-one-dimensional regime, which is characterized by  $\hbar\omega_\rho \gg \hbar\omega_z$ , but not the truly one-dimensional regime. Quasi-one-dimensional trapping confinement has also been realized utilizing optical lattices [18] and wave guides [19,20]. Although experimental techniques will advance further, there will always be an upper limit on the ratio  $a_\rho/a_z$ . The natural question then is under what conditions does the system behave truly one-dimensional, or, to which extent is the motion in the tight confinement directions decoupled from the motion in the weak confinement direction.

Various authors have studied the crossover from the three-dimensional regime to the Tonks regime. Common to these studies is some sort of variable separation of the tight and loose confinement directions [10,11,13,21–24]. For a cylindrical trap, e.g., Dunjko *et al.* [10] solve the Schrödinger equation by employing the Lieb-Liniger model [3] and a local density approximation. For a toroidal trap, in contrast, Das *et al.* [13] develop a variational theory that factorizes the wave function into a longitudinal and a transverse part. Our approach here is different in spirit, in that it treats the  $3N$ -dimensional Hamiltonian using the diffusion quantum Monte Carlo (DMC) technique [25–28] fully quantum mechanically and nonperturbatively. Thus, no separation of variables needs to be made, and our results could be used to benchmark variational calculations.

The DMC method has been previously applied to microscopic Bose-Einstein condensates (BECs) under spherical confinement [29] (for applications of Monte Carlo techniques to gaseous condensates see [30–34]). Similarly to Ref. [29], we monitor the ground state energy and structural properties as a function of the number of particles. In addition, we vary the aspect ratio over a wide range, i.e.,  $L = 1, \dots, 10000$ , which allows signatures of fermionization to be investigated. Importantly, our approach includes correlation effects explicitly by treating all  $3N$  coordinates of the system equivalently.

Section II outlines the DMC formalism and describes the system under study, while Sec. III presents our results for the energetics and structural properties. Finally, Sec. IV concludes.

## II. NUMERICAL TECHNIQUES AND CHARACTERIZATION OF THE SYSTEM

### A. Diffusion quantum Monte Carlo technique

The DMC method shows a favorable scaling with the number  $N$  of particles, and allows bosonic many-body systems to be treated fully quantum mechanically and nonperturbatively. The DMC method [25–28] solves the *time-independent* Schrödinger equation

$$H\varphi_n = E_n\varphi_n \quad (1)$$

for its ground state,  $n = 0$ , by considering the *time-dependent* Schrödinger equation. Introduction of imaginary time  $\tau = it/\hbar$  is used to remove the explicit dependence on “ $i$ ”,

$$\frac{\partial\Psi(\vec{r},\tau)}{\partial\tau} = \underbrace{\frac{\hbar^2}{2m}\sum_{j=1}^N\nabla_j^2\Psi(\vec{r},\tau)}_{\text{diffusion}} - \underbrace{[V(\vec{r}) - E_{ref}]\Psi(\vec{r},\tau)}_{\text{source/sink}}. \quad (2)$$

Here,  $\vec{r} = (\vec{r}_1, \dots, \vec{r}_N)$  collectively denotes the nuclear Cartesian coordinates of the atoms in the trap.  $V(\vec{r})$  is the potential energy surface of the system, which is assumed to be known for now.  $E_{ref}$  shifts the absolute energy scale without changing the solution to the time-independent Schrödinger equation, Eq. (1).

A random walk technique is then used to calculate the steady state solution [eigenvector  $\varphi_0(\vec{r})$  with eigenvalue  $E_0$ ] by propagating to large  $\tau$ :  $\lim_{\tau \rightarrow \infty} \Psi(\vec{r}, \tau) \rightarrow \varphi_0(\vec{r})$ . Typically, about 1000 “walkers” are simulated simultaneously. A walker is characterized by its position in Cartesian space and a weight factor indicating its “importance”. To perform the propagation in imaginary time  $\tau$ , the short-time approximation to the Green’s function is introduced, and the kinetic energy part (“diffusion”) and the potential energy part (“source/sink”) of the Hamiltonian are simulated separately at each time step  $\Delta\tau$ .

The DMC algorithm outlined in the previous paragraphs is often referred to as DMC *without importance sampling* or DMC *with a constant trial wave function*. It turns out that a trial wave function  $\psi_T(\vec{r})$  that approximates the true ground state wave function  $\varphi_0(\vec{r})$ , can be exploited fruitfully for increased accuracy. Introduction of  $\psi_T$  does not change the solution to the time-independent Schrödinger equation [Eq. (1)]; however, it does give an additional term (“drift”) in the time-dependent Schrödinger equation,

$$\begin{aligned} \frac{\partial(\Psi\psi_T)}{\partial\tau} = & \underbrace{\frac{\hbar^2}{2m}\sum_{j=1}^N\nabla_j^2(\Psi\psi_T)}_{\text{diffusion}} - \underbrace{\frac{\hbar^2}{m}\sum_{j=1}^N\nabla_j(\Psi\psi_T\nabla\ln\psi_T)}_{\text{drift}} \\ & - \underbrace{\left[\frac{-\hbar^2}{2m}\psi_T^{-1}\left(\sum_{j=1}^N\nabla_j^2\psi_T\right) + V(\vec{r}) - E_{ref}\right]}_{\text{source/sink}}(\Psi\psi_T). \end{aligned} \quad (3)$$

At each time step  $\Delta\tau$ , the new drift (or force) term introduces an additional update of the Cartesian coordinates of the walkers. Incorporation of a “good” trial wave function  $\psi_T$ , namely one that resembles the true ground state wave function  $\varphi_0(\vec{r})$  as closely as possible, leads to a large reduction of the time step error of the DMC calculation [35–38]. A “bad” trial wave function, in contrast, can lead to biased sampling of the configuration space, and can, in the worst case, lead to a seemingly stable solution that differs from the true, stationary solution of the time-independent Schrödinger equation, Eq. (1). Incorporation of a trial wave function  $\psi_T$  is required in the present application to obtain converged DMC results. The algorithm with a non-constant trial wave function is typically referred to as DMC *with importance sampling*.

The DMC algorithm results in an estimate of the ground state energy  $E_0$ , which is accompanied by a systematic time step error and additional statistical noise due to the stochastic nature of the simulation process. The time step error can be reduced by performing a series of calculations for different time steps  $\Delta\tau$ , and then extrapolating  $E_0(\Delta\tau)$  to the zero time step limit  $\Delta\tau = 0$ . The statistical noise of the energy expectation value can be reduced by performing longer simulation runs.

The calculation of structural ground state properties requires a little more care than the calculation of the ground state energy because Eq. (2) interprets the wave function itself as the density of the system, whereas Eq. (3) interprets

the product  $\Psi\psi_T$  as the density of the system (see also Sec. II B). To obtain structural properties, such as the radial distribution, from the DMC simulation with importance sampling, one therefore either uses approximate mixed estimators or employs essentially exact extrapolation techniques such as descendant weighting [39–41]. The latter is employed in the present application.

## B. Application to trapped atomic gases

This section discusses the application of the outlined DMC formalism with importance sampling to trapped bosonic gases. The DMC method “interprets” the wave function of the system as its density, and its application is thus restricted to bosonic systems with a positive and nodeless wave function [42]. What are the implications for treating condensed atomic gases by the DMC method? Ideally, one would like to simulate a condensate using a sum of “exact” two-body atom-atom interaction potentials, e.g., the Krauss-Stevens Rb-Rb potential [43] (and possibly three-body terms), however, it is well known that the ground state of such a many-body interaction potential corresponds to a “metallic snowflake-like” state. The gaseous condensate state is not the ground state of the system but a highly-excited metastable state with a finite lifetime. To treat metastable condensates by the DMC method we artificially modify the two-body interaction potential so that the gas-like BEC state becomes the ground state.

The full potential surface of the  $N$  atom system is composed of an internal and an external piece. We parameterize the interatomic many-body potential surface by a sum of two-body potentials  $V_2$ ,  $\sum_{j>k} V_2(r_{kj})$ , where  $r_{kj}$  denotes the distance between atom  $k$  and atom  $j$ ,  $r_{kj} = |\vec{r}_j - \vec{r}_k|$ . In addition, each atom feels the cigar-shaped external confining potential  $V_{trap}(\vec{r}_k) = \frac{1}{2}m(\omega_\rho^2\rho_k^2 + \omega_z^2z_k^2)$ . Our many-body Hamiltonian  $H$  for  $N$  mass  $m$  atoms then becomes

$$H = -\frac{\hbar^2}{2m} \sum_{j=1}^N \nabla_j^2 + \sum_{j>k,k=1}^N V_2(r_{kj}) + \sum_{j=1}^N V_{trap}(\vec{r}_j), \quad (4)$$

where the Cartesian position vector  $\vec{r}_j = (x_j, y_j, z_j)$  is measured with respect to the center of the trap. Our calculations are performed for a simple two-body hardcore potential,  $V_2(r_{kj}) = \infty$  for  $r_{kj} < a$ , and  $V_2(r_{kj}) = 0$  otherwise, where  $a$  denotes the two-body  $s$ -wave scattering length [29–34,44,45].

Our trial wave function  $\psi_T$  is chosen to have the simple Bijl-Jastrow-type form [46,47],

$$\psi_T(\vec{r}_1, \dots, \vec{r}_N) = \left( \prod_{j>k,k=1}^N \phi(r_{kj}) \right) \times \left( \prod_{l=1}^N \Phi(\vec{r}_l) \right), \quad (5)$$

which has the proper symmetry for a bosonic system, namely, exchange of two particles leaves  $\psi_T$  unchanged.  $\phi(r_{kj})$  is determined by the solution to the radial two-body scattering equation for  $V_2(r_{kj})$ . For the hardcore potential, one obtains  $\phi(r_{kj}) = (1 - a/r_{kj})$  for  $r_{kj} > a$ , and  $\phi(r_{kj}) = 0$  otherwise. Thus,  $\phi$  prevents two atoms from “crashing into each other”. In contrast,  $\Phi$  is the part of  $\psi_T$  that keeps the atoms inside the trap.  $\Phi(\vec{r}_l)$  has two variational parameters,  $p_1$  and  $p_2$ ,

$$\Phi(\vec{r}_l) = \exp \left[ -\frac{1}{2} (\rho_l/a_\rho)^2 - p_1 (z_l/a_z)^{p_2} \right]. \quad (6)$$

We determine the best parameters  $p_1$  and  $p_2$  by minimizing the energy expectation value  $\langle \psi_T | H | \psi_T \rangle / \langle \psi_T | \psi_T \rangle$  through variational quantum Monte Carlo (VMC) calculations [27,34]. For an ideal bosonic gas ( $a = 0$ ),  $p_1 = 1/2$  and  $p_2 = 2$ , while for  $a > 0$ , the optimal values for  $p_1$  and  $p_2$  depend on  $a$ ,  $N$ , and the strength of the confining potential.

Our calculations are performed for  $N = 2, \dots, 20$  with  $m = m(^{87}\text{Rb})$ ,  $\nu_z = 77.78\text{Hz}$ , a two-body  $s$ -wave scattering length  $a = 100\text{a.u.}$ , and varying  $\nu_\rho$ ,  $\nu_\rho = 1\nu_z, \dots, 10000\nu_z$ . The DMC calculations become increasingly demanding with increasing aspect ratio  $L = \nu_\rho/\nu_z$ , since the strength of the tight confining direction predominantly determines the timestep  $\Delta\tau$ . To ensure an acceptance rate of over 98% in the acceptance/rejection step of the DMC algorithm [27],  $\Delta\tau$  has to be decreased with increasing  $\nu_\rho$  as it scales roughly with  $a_\rho$ . Thus, to achieve the same total propagation time for a system with  $L = 1$  and for a system with  $L = 10000$ , we need to perform about two orders of magnitude more propagation steps for the system with  $L = 10000$  than for the system with  $L = 1$ .

The number of propagation steps also determines to first order the statistical uncertainty of any quantity calculated by the DMC technique. Assume we wish to determine DMC energies with a statistical uncertainty of  $< 0.2\hbar\omega_z$ . For a bosonic gas with  $N = 10$  atoms, e.g., this implies an accuracy of about 1% for  $L = 1$ , and of about  $4 \times 10^{-4}\%$  for  $L = 10000$ . Achieving convergence of structural properties is more demanding than achieving convergence of

the ground state energy. The descendant weighting technique [39–41] employed here requires a delay between the “original sampling” and the “sampling that is being used for reweighting purposes”. To obtain converged structural properties, this delay is as big as 10000 for some of our simulations.

### III. RESULTS

This section presents our DMC results. Section III A summarizes energetics, while Sec. III B discusses structural properties. Section III C relates our results to those by Petrov *et al.* [8] and by Dunjko *et al.* [10].

#### A. Energetics

Figure 1 shows our DMC ground state energies  $E_0^{DMC}$  (diamonds; for each  $N$ , dotted lines connect the DMC energies to guide the eye) in units of  $\hbar\omega_z$  as a function of the aspect ratio  $L$  on a log-log scale for  $N = 3, 5, 10$  and  $20$ .  $L$  extends over four orders of magnitude, and  $E_0^{DMC}$  over about five orders of magnitude. The statistical uncertainty of  $E_0^{DMC}$  is smaller than the symbol size. Figure 1 also shows the ground state energies  $E_0^{GP}$  (triangles) [48] obtained by solving the mean-field Gross-Pitaevskii (GP) equation [49–51] in cylindrical coordinates with interaction parameter  $\alpha = (N - 1)a$ ,

$$\left[ -\frac{\hbar^2}{2m}\nabla^2 + \frac{1}{2}m(\omega_\rho^2\rho^2 + \omega_z^2z^2) + \frac{4\pi\hbar^2}{m}\alpha|\chi_0(\rho, \varphi, z)|^2 \right] \chi_j(\rho, \varphi, z) = \epsilon_j\chi_j(\rho, \varphi, z). \quad (7)$$

The definition of  $\alpha$  stems from the derivation of the GP equation based on the Hartree-Fock formalism [52].  $\epsilon_j$  and  $\chi_j$  denote the orbital energy and the orbital wave function, respectively; the GP ground state energy  $E_0^{GP}$  can be obtained from the energy functional  $E_0^{GP}[\chi_0]$ . The numerical solution of Eq. (7) can be simplified by separating out the motion in the  $\varphi$  coordinate. On the scale of Fig. 1, the DMC and GP energies are indistinguishable.

To interpret our results, we subtract the ideal bosonic gas energy in the tight confinement direction,  $E_0^{B,\rho} = Nh\nu_\rho$ , from our DMC [GP] ground state energies, and denote the resulting energies by  $E_0^{DMC,z}$  [ $E_0^{GP,z}$ ]. Figure 2 shows  $E_0^{DMC,z}/N$  (diamonds) as a function of  $L$  on a logarithmic scale. To guide the eye, dotted lines connect our data for each  $N$ . The statistical uncertainty of the DMC energies  $E_0^{DMC,z}$  increases with increasing aspect ratio  $L$ . E.g., the ground state energy of a gas with  $N = 5$  and  $L = 10$  is  $E_0^{DMC} = 52.838(2)h\nu_z$ . Subtracting the ideal gas energy in the  $\rho$  direction,  $E_0^{B,\rho} = 50h\nu_z$ , gives a value of  $E_0^{DMC,z} = 2.838(2)h\nu_z$  with an uncertainty of  $0.002h\nu_z$ . For  $L = 10000$ , we find  $E_0^{DMC,z} = 12.4(2)h\nu_z$ , a 100 times larger statistical uncertainty. Reducing the statistical uncertainty for  $L = 10000$  from  $0.2h\nu_z$  to  $0.002h\nu_z$  is possible in principle, however, would require significantly more computer time.

For comparison, Fig. 2 also shows the GP energies  $E_0^{GP,z}/N$  in the  $z$  coordinate only (triangles; for each  $N$ , dotted lines connect these points to guide the eye). For small  $L$ , the many-body DMC energies  $E_0^{DMC,z}/N$  and the GP energies  $E_0^{GP,z}/N$  agree well as expected. However, as  $L$  increases, significant deviations occur. These deviations are a consequence of considering the energy in the  $z$  direction only (see also Sec. III B); the deviations between the total DMC and GP energies,  $E_0^{DMC}$  and  $E_0^{GP}$ , are negligibly small (see Fig. 1). As we discuss now, Fig. 2 confirms that the systems under study undergo fermionization for large  $L$  as suggested by several authors [8,10,13].

Solid horizontal lines on the right hand side of Fig. 2 indicate the energy in the Tonks limit,  $E_0^{F,z}/N = Nh\nu_z/2$ . For each  $N$  [53], our DMC energies  $E_0^{DMC,z}/N$  approach the Tonks energy, suggesting that the simulation parameters are such that the considered systems behave *fermionic* in the  $z$  direction, while the motion in the  $\rho$  direction is frozen out. Importantly, our simulations are performed using a trial wave function  $\psi_T$ , Eq. (5), with the proper bose symmetry for all  $L$ .

To illustrate the fermionization transition further, the lower part of Fig. 3 shows the DMC energies  $E_0^{DMC,z}$  divided by the Fermi energies  $E_0^{F,z}$  as a function of  $L$  (diamonds) on a logarithmic scale for  $N = 2, 3, 5, 10$  and  $20$ . For each  $N$ , this ratio is close to zero for small  $L$ , and approaches one as  $L$  increases. The  $N = 2$  system approaches the Tonks limit at smaller  $L$  values than the  $N = 20$  system. In addition, the upper part of Fig. 3 shows the ratio between the DMC energies  $E_0^{DMC,z}$  and the ideal bosonic gas energy in the  $z$  direction,  $E_0^{B,z}$  (triangles). For each  $N$ , this ratio is close to one at small  $L$ , and increases with increasing  $L$ . In summary, the energy ratios shown in Fig. 3 indicate that atomic gases under cigar-shaped confinement behave predominantly *bosonic* for small  $L$  and predominantly *fermionic* for large  $L$ .

Our analysis in this section depends profoundly on subtracting the ideal bosonic gas energy in the  $\rho$  direction from the many-body energy. The next section discusses structural properties, for which the behavior in the  $\rho$  direction and

in the  $z$  direction can be *naturally* separated by integrating over all coordinates but the coordinate of interest, i.e., without making any approximations.

## B. Structural properties

Figure 4 shows the DMC density  $n_0^{DMC,\rho}$ , normalized such that  $\int_0^\infty n_0^{DMC,\rho}(\rho)d\rho = 1$ , for  $N = 5$  for two different aspect ratios, i.e.,  $L = 10$  (diamonds) and  $L = 10000$  (triangles). The  $\rho$  coordinate is measured in units of  $a_\rho^{-1}$  with  $a_\rho = 7307$ a.u. for  $L = 10$ , and  $a_\rho = 231$ a.u. for  $L = 10000$ , respectively (see Tab. I). The statistical uncertainty of  $n_0^{DMC,\rho}$  is largest for small  $\rho$  since the DMC walk samples the small  $\rho$  region less than the large  $\rho$  region. A solid line shows the density for the ideal bosonic gas,

$$n_0^{B,\rho}(\rho) = \frac{2}{\sqrt{\pi}a_\rho} \exp[-(\rho/a_\rho)^2]. \quad (8)$$

On the scale of Fig. 4, the DMC densities and the ideal gas density are indistinguishable, which suggests that the motion along the  $\rho$  coordinate is indeed frozen out as  $L$  approaches large values (see Sec. III A).

The density along the  $z$  coordinate is more interesting than the density along the  $\rho$  coordinate, since its behavior changes dramatically as a function of the aspect ratio  $L$ . Figure 5 shows the DMC density  $n_0^{DMC,z}(z)$ , normalized such that  $\int_{-\infty}^\infty n_0^{DMC,z}(z)dz = 1$ , for  $N = 3$  for four different aspect ratios  $L$ , i.e.,  $L = 10$  (diamonds), 100 (crosses), 1000 (triangles), and 10000 (stars).  $z$  is measured in units of  $a_z^{-1}$ , where  $a_z = 23107$ a.u.. For each  $L$ , dotted lines connect the symbols to guide the eye. Additionally, a solid grey line shows the one-dimensional ideal bosonic gas density  $n_0^{B,z}$ ,

$$n_0^{B,z}(z) = \frac{1}{\sqrt{\pi}a_z} \exp[-(z/a_z)^2]. \quad (9)$$

A solid dark line shows the ideal fermionic gas density  $n_0^{F,z}$ , which is given by the sum of squares of the single-particle wave functions,

$$n_0^{F,z}(z) = \frac{1}{N} \frac{1}{\sqrt{\pi}a_z} \sum_{k=0}^{N-1} \frac{1}{2^k k!} H_k^2(z/a_z) \exp[-(z/a_z)^2], \quad (10)$$

where the  $H_k$  denote Hermite polynomials. The Fermi density shows three distinct maxima, corresponding to  $N = 3$ .

To ensure an unbiased observation of the fermionization effect in our DMC calculations, we choose a “structureless” trial wave function  $\psi_T$ , that is a trial wave function without oscillations. Figure 6 shows the  $z$  component of  $\psi_T$  squared (grey solid line),

$$M \exp[-2p_1(z/a_z)^{p_2}], \quad (11)$$

with  $p_1 = 0.018$  and  $p_2 = 4.43$  ( $M$  is a properly chosen normalization constant), together with the DMC density for  $L = 10000$  and  $a = 100$ a.u. (diamonds) and the ideal fermionic gas density [Eq. (10), black solid line]. We checked the “delay” employed in the descendant weighting scheme of our DMC calculation (see Sec. II B), and estimate the statistical uncertainty to be about three times the symbol size. The DMC density for  $L = 10000$  does not seem to show any Fermi-oscillations (note, however, that the statistical error of the DMC density is non-negligible, as indicated exemplarily for one data point at  $z = 1a_z^{-1}$ ).

Based on a single-particle picture, Petrov *et al.* [8] and Dunjko *et al.* [10] derive an expression for the density of a gas under cylindrical confinement in the Tonks limit,

$$n_0^{Tonks}(z) = \sqrt{\frac{2}{\pi^2 N a_z^2} \left(1 - \frac{z^2}{2N a_z^2}\right)^{1/2}}. \quad (12)$$

Notably,  $n_0^{Tonks}$  is dependent on  $N$  and  $a_z$  only, i.e., it is independent of  $a$ . Figure 6 indicates that  $n_0^{Tonks}$  (dashed line) follows the Fermi density [Eq. (10), dark solid line] closely, except for the oscillations, which cannot be described within a single-particle picture. The DMC density  $n_0^{DMC,z}$  agrees well with  $n_0^{Tonks}$ . Section III C presents a detailed comparison between our work and that by Petrov *et al.* [8] and by Dunjko *et al.* [10].

The Fermi density, Eq. (10), changes significantly with increasing  $N$ . To illustrate this effect, Fig. 7 shows the DMC density  $n_0^{DMC,z}$  as a function of  $z$  for  $N = 10$  for three different  $L$  values,  $L = 10$  (diamonds), 100 (crosses), and 1000 (diamonds), using the same scale as in Fig. 5 for  $N = 3$ . The Fermi density (dark solid line) now shows ten maxima, owing to the increased number of terms in Eq. (10). As  $L$  increases the DMC density approaches the Fermi density. Our density studies, discussed here in detail for  $N = 3$  and  $N = 10$ , support our interpretation of the energetics presented in Sec. III A, and show strong evidence that an atomic gas under external confinement indeed undergoes fermionization as  $L$  increases.

### C. Comparisons with the literature

This section relates our results to a set of criteria put forward by Petrov *et al.* [8] and by Dunjko *et al.* [10]. Dunjko *et al.* [10] derive five requirements for a successful experimental observation of the zero-temperature Tonks gas density profile, Eq. (12).

1.  $a$  positive and  $C1 = \frac{C}{\sqrt{2}} \frac{a}{a_\rho} < 1$ , where  $C \approx 1.4603$ . These conditions imply a positive one-dimensional coupling constant  $g_{1d}$ ,

$$g_{1d} = -\frac{2\hbar^2}{ma_{1d}} \quad \text{with} \quad a_{1d} = -\frac{a_\rho^2}{a} \left(1 - \frac{C}{\sqrt{2}} \frac{a}{a_\rho}\right). \quad (13)$$

2.  $C2 = \frac{\hbar\omega_z N}{\hbar\omega_\rho} \ll 1$ . The transverse energy level spacing must exceed the energy of the gas in the  $z$  direction.
3.  $C3 = \eta \ll 1$ , where  $\eta$  denotes the governing parameter of the system,

$$\eta = \frac{(9/2)^{1/3}}{8} \left[ \frac{4a_\rho^4 \left(1 - \frac{C}{\sqrt{2}} \frac{a}{a_\rho}\right)^2}{a^2 a_z^2} \right]^{2/3} N^{2/3}. \quad (14)$$

4.  $C4 = \frac{\hbar\omega_z}{2\hbar^2/(ma_{1d}^2)} \ll 1$ . The energy  $\frac{2\hbar^2}{ma_{1d}^2}$  must exceed the energy level spacing in the  $z$  direction.
5.  $N > 1$ . This condition is fulfilled trivially.

Table I summarizes the characteristic lengths  $a_\rho$  and the one-dimensional scattering lengths  $a_{1d}$  as a function of  $L$  for  $a = 100$  a.u.,  $m = m(^{87}\text{Rb})$ , and  $\nu_z = 77.78$  Hz. Condition 1. puts an upper limit on the aspect ratio  $L$ ; for the parameters chosen here, the coupling constant  $g_{1d}$  becomes negative ( $a_{1d}$  becomes positive) for  $L \approx 50000$ .  $C1$  and  $C4$  are independent of  $N$ , while  $C2$  and  $C3$  scale with  $N$  and  $N^{2/3}$ , respectively.

Figure 8 shows the criteria  $C1$  through  $C4$  as a function of  $L$  on a log-log scale.  $C2$  and  $C3$  are shown for  $N = 3$ , and 20.  $C2 - C4$  are smaller than 0.1 for about  $L > 3500$ , and smaller than 0.01 for the extreme aspect ratio of about  $L > 20000$ . The behavior of  $C2$  and  $C3$  indicates that the “window”, in which an atomic gas behaves like a Tonks gas, becomes narrower as  $N$  increases. It thus seems advantageous to experimentally work with small particle samples. Toward this end, optical lattices [18,54], which allow preparation of several 1000 identical copies of microscopic atom samples, seem most promising. Additionally tuning the two-body  $s$ -wave scattering length to large positive values through the use of Feshbach resonances [55,56] would move the transition to the Tonks regime to smaller aspect ratios. A critical question, which is beyond the scope of this paper, is whether the density profile in the  $z$  direction can be unambiguously measured in time-of-flight expansion experiments, or whether mean-field effects may mask the signature of the Tonks density profile [22,23,57].

## IV. SUMMARY AND OUTLOOK

The present DMC studies of atomic gases under external confinement with varying aspect ratio provide first benchmark results, which will allow the accuracy of numerically less demanding, and more commonly used approximate approaches to be tested. In contrast to variable separation schemes and mean-field-type approaches, the DMC formalism treats many-body correlations explicitly. The DMC method consistently treats atomic gases under spherical confinement and under highly-elongated cylindrical confinement, and thus allows the transition from three-dimensional

to one-dimensional to be mapped out uniquely. Application of the DMC technique can be extended to arbitrary confining potentials such as toroidal or random potentials. The main modification of the DMC algorithm would amount to adjusting the  $\Phi$  component of the trial wave function, Eqs. (5) and (6), accordingly.

The DMC method in its present implementation is restricted to treating many-body systems in their ground state. To nevertheless treat metastable atomic gases, the present study parameterizes the atom-atom interaction potential by a simple repulsive model potential, i.e., a hardcore potential. It would be interesting to investigate dependencies of the energetics and structural properties on the detailed shape of the two-body interaction potential as a function of the aspect ratio  $L$ . Of particular interest would be the characterization of atomic gases under external confinement as a function of the ratios  $a/a_z$  and  $b/a_z$ , where  $b$  denotes the characteristic length of the two-body potential [58–60].

The application of the zero-temperature DMC technique in its present implementation is restricted to a description of *static properties*: We cannot make predictions regarding the lifetime or stability of trapped atomic gases. Our studies here characterize atomic gases, assuming that they are stable. Our approach provides no access to information related to finite temperature effects, time evolution, and coherence/decoherence phenomena.

In summary, this paper presents exact many-body calculations for trapped atomic bosonic gases under external confinement with varying aspect ratio. The trapping geometries considered range from spherical to highly elongated,  $L = 1 - 10000$ . The DMC technique is powerful in assessing the importance of many-body correlations. Our study provides first benchmark results for atomic gases under highly elongated cylindrical confinement.

## ACKNOWLEDGMENTS

Fruitful discussions with Chris H. Greene at an early stage of this project are gratefully acknowledged. I thank Brett D. Esry for providing numerical solutions to the two-dimensional Gross-Pitaevskii equation.

- 
- [1] L. Tonks, Phys. Rev. **50**, 955 (1936).
- [2] M. Girardeau, J. Math. Phys. **1**, 516 (1960).
- [3] E. H. Lieb and W. Liniger, Phys. Rev. **130**, 1605 (1963).
- [4] E. H. Lieb, Phys. Rev. **130**, 1616 (1963).
- [5] M. Olshanii, Phys. Rev. Lett. **81**, 938 (1998).
- [6] A. G. Rojo, J. L. Cohen, and P. R. Berman, Phys. Rev. A **60**, 1482 (1999).
- [7] M. D. Girardeau and E. M. Wright, Phys. Rev. Lett. **84**, 5239 (2000).
- [8] D. S. Petrov, G. V. Shlyapnikov, and J. T. M. Walraven, Phys. Rev. Lett. **85**, 3745 (2000).
- [9] E. B. Kolomeisky, T. J. Newman, J. P. Straley, and X. Qi, Phys. Rev. Lett. **85**, 1146 (2000).
- [10] V. Dunjko, V. Lorent, and M. Olshanii, Phys. Rev. Lett. **86**, 5413 (2001).
- [11] M. D. Girardeau and E. M. Wright, Phys. Rev. Lett. **87**, 210401 (2001).
- [12] M. D. Girardeau, E. M. Wright, and J. M. Triscari, Phys. Rev. A **63**, 033601 (2001).
- [13] K. K. Das, M. D. Girardeau, and E. M. Wright, cond-mat/0204317 v1 15 Apr 2002.
- [14] A. Görlitz *et al.*, Phys. Rev. Lett. **87**, 130402 (2001).
- [15] S. Dettmer *et al.*, Phys. Rev. Lett. **87**, 160406 (2001).
- [16] F. Schreck *et al.*, Phys. Rev. Lett. **87**, 080403 (2001).
- [17] K. E. Strecker, G. B. Partridge, A. G. Truscott, and R. G. Hulet, Nature **417**, 150 (2002).
- [18] M. Greiner *et al.*, Phys. Rev. Lett. **87**, 160405 (2001).
- [19] J. H. Thywissen *et al.*, Eur. Phys. J. D **7**, 361 (1999).
- [20] K. Bongs *et al.*, Phys. Rev. A **63**, 031602(R) (2001).
- [21] B. Tanatar, Europhys. Lett. **51**, 261 (2000).
- [22] P. Massignan and M. Modugno, cond-mat/0205516 v1 24 May 2002.
- [23] C. Menotti and S. Stringari, cond-mat/0201158 v1 10 Jan 2002.
- [24] L. Salasnich, A. Parola, and L. Reatto, Phys. Rev. A **65**, 043614 (2002).
- [25] J. B. Anderson, J. Chem. Phys. **63**, 1499 (1975).
- [26] P. J. Reynolds, J. Tobochnik, and H. Gould, Comput. Phys. **4**, 662 (1990).
- [27] B. L. Hammond, W. A. Lester, Jr., and P. J. Reynolds, *Monte Carlo Methods in Ab Initio Quantum Chemistry* (World Scientific, Singapore, 1994).
- [28] I. Kosztin, B. Faber, and K. Schulten, Am. J. Phys. **64**, 633 (1996).
- [29] D. Blume and C. H. Greene, Phys. Rev. A **63**, 063601 (2001).
- [30] W. Krauth, Phys. Rev. Lett. **77**, 3695 (1996).
- [31] P. Grüter, D. Ceperley, and F. Laloë, Phys. Rev. Lett. **79**, 3549 (1997).
- [32] S. Pearson, T. Pang, and C. Chen, Phys. Rev. A **58**, 1485 (1998).
- [33] S. Giorgini, J. Boronat, and J. Casulleras, Phys. Rev. A **60**, 5129 (1999).
- [34] J. L. DuBois and H. R. Glyde, Phys. Rev. A **63**, 023602 (2001).
- [35] K. McDowell, Int. J. Quantum Chem. Symp. **15**, 177 (1981).
- [36] R. Bianchi, P. Cremaschi, G. Morosi, and C. Puppi, Chem. Phys. Lett. **148**, 86 (1988).
- [37] S. A. Chin, Phys. Rev. A **42**, 6991 (1990).
- [38] C. J. Umrigar, M. P. Nightingale, and K. J. Runge, J. Chem. Phys. **99**, 2865 (1993).
- [39] M. H. Kalos, J. Comput. Phys. **2**, 257 (1967).
- [40] K. S. Liu, M. H. Kalos, and G. V. Chester, Phys. Rev. A **10**, 303 (1974).
- [41] R. N. Barnett, P. J. Reynolds, and W. A. Lester, Jr., J. Comput. Phys. **96**, 258 (1991).
- [42] Modifications of the DMC algorithm exist that allow treatment of excited states, however, their application to gaseous condensates is non-trivial.
- [43] M. Krauss and W. J. Stevens, J. Chem. Phys. **93**, 4236 (1990).
- [44] K. Huang and C. N. Yang, Phys. Rev. **105**, 767 (1957).
- [45] T. D. Lee, K. Huang, and C. N. Yang, Phys. Rev. **106**, 1135 (1957).
- [46] A. Bijl, Physica **7**, 869 (1940).
- [47] R. Jastrow, Phys. Rev. **98**, 1479 (1955).
- [48] The numerical solutions to the two-dimensional Gross-Pitaevskii equation were kindly provided by B. D. Esry.
- [49] E. P. Gross, Nuovo Cimento **20**, 454 (1961).
- [50] L. P. Pitaevskii, J. Exptl. Theoret. Phys. (U.S.S.R.) **40**, 646 (1961).
- [51] F. Dalfovo, S. Giorgini, L. P. Pitaevskii, and S. Stringari, Rev. Mod. Phys. **71**, 463 (1999).
- [52] B. D. Esry, Phys. Rev. A **55**, 1147 (1997).
- [53] Obtaining convergence for systems with  $N = 20$  and large  $L$  is numerically demanding. In this paper we only report results for  $L \leq 200$ .
- [54] M. Greiner *et al.*, Nature **415**, 39 (2002).
- [55] P. Courteille *et al.*, Phys. Rev. Lett. **81**, 69 (1998).
- [56] S. Inouye *et al.*, Nature **392**, 151 (1998).
- [57] P. Öhberg and L. Santos, cond-mat/0204611 v1 29 Apr 2002.
- [58] G. F. Gribakin and V. V. Flambaum, Phys. Rev. A **48**, 546 (1993).
- [59] B. Gao, Phys. Rev. A **58**, 4222 (1998).
- [60] D. Blume and C. H. Greene, Phys. Rev. A **65**, 043613 (2002).

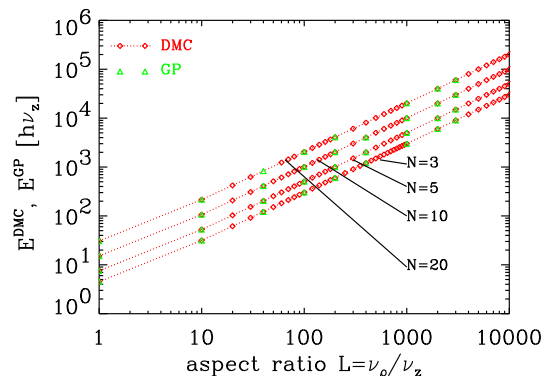


FIG. 1. Ground state DMC energy,  $E_0^{DMC}$  (diamonds; for each  $N$ , dotted lines connect the DMC energies to guide the eye), together with the ground state energy obtained by solving the two-dimensional Gross-Pitaevskii equation,  $E_0^{GP}$  (triangles), as a function of the aspect ratio  $L = \nu_\rho/\nu_z$  on a log-log scale for  $N = 3, 5, 10$  and  $20$ . The statistical errorbar of the DMC energies is smaller than the symbol size.

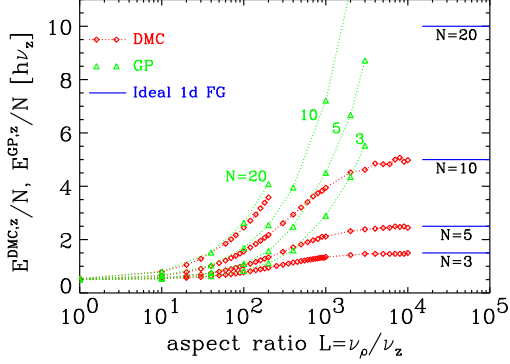


FIG. 2. Energy per particle along the  $z$  coordinate only. The DMC energies  $E_0^{DMC,z}/N$  (diamonds) are shown together with the GP energies  $E_0^{GP,z}/N$  (triangles) as a function of the aspect ratio  $L$  on a logarithmic scale for  $N = 3, 5, 10$  and  $20$ . To guide the eye, dotted lines connect the DMC and GP energies for each  $N$ . Clear discrepancies between  $E_0^{DMC,z}/N$  and  $E_0^{GP,z}/N$  are visible at larger  $L$ . Horizontal solid lines on the right hand side show the energies in the Tonks limit,  $E_0^{F,z}/N$ .

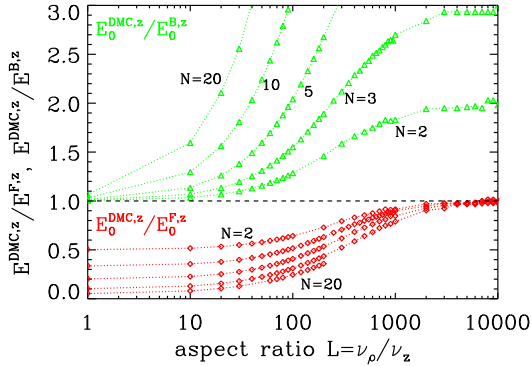


FIG. 3. Ratio between the DMC energy in the  $z$  direction and the Tonks energy,  $E_0^{DMC,z}/E_0^{F,z}$  (lower part, diamonds) as a function of  $L$  on a logarithmic scale, together with the ratio  $E_0^{DMC,z}/E_0^{B,z}$  (upper part, triangles) for  $N = 2, 3, 5, 10$  and  $20$ . As  $L$  increases the ratio  $E_0^{DMC,z}/E_0^{F,z}$  approaches one, while the ratio  $E_0^{DMC,z}/E_0^{B,z}$  approaches values much greater than one, i.e., the value  $N$ , indicating that the confined atomic gas undergoes fermionization as  $L$  increases.

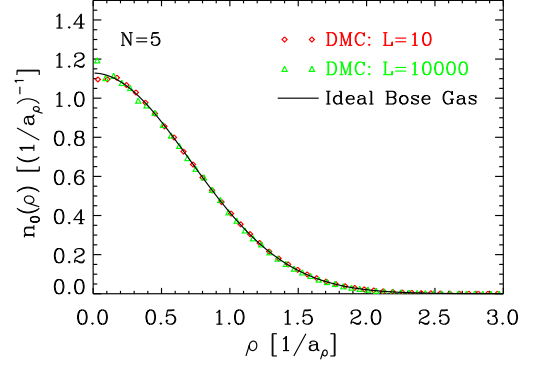


FIG. 4. DMC density  $n_0^{DMC,\rho}$  as a function of  $\rho$  for  $N = 5$  for two different aspect ratios  $L$ ,  $L = 10$  (diamonds) and  $L = 10000$  (triangles). To collapse the two DMC densities onto the same scale,  $\rho$  is measured in units of  $a_\rho^{-1}$  with  $a_\rho = 7307\text{a.u.}$  for  $L = 10$ , and  $a_\rho = 231\text{a.u.}$  for  $L = 10000$ , respectively. Additionally, a solid line shows the ideal bosonic gas density [Eq. (8)]. The DMC densities follow the ideal bosonic gas density closely.

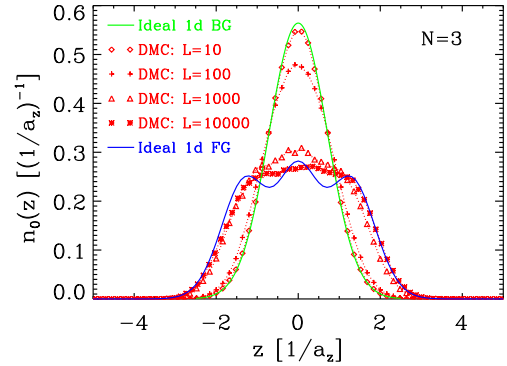


FIG. 5. DMC density  $n_0^{DMC,z}$  for  $N = 3$  as a function of  $z$  for four different aspect ratios,  $L = 10$  (diamonds),  $100$  (crosses),  $1000$  (triangles), and  $10000$  (stars).  $z$  is measured in units of  $a_z^{-1}$ , where  $a_z = 23107\text{a.u.}$ . In addition, a grey solid line shows the ideal gas density for bosons [Eq. (9)], and a dark solid line shows that for fermions [Eq. (10)]. The DMC density is close to  $n_0^{B,z}$  for small  $L$ , and approaches  $n_0^{F,z}$  as  $L$  increases.

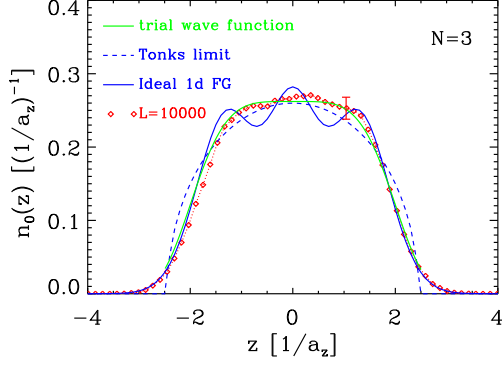


FIG. 6. DMC density  $n_0^{DMC,z}$  for  $N = 3$  as a function of  $z$  for  $L = 10000$  (diamonds; the statistical uncertainty is indicated exemplary for  $z = 1/a_z^{-1}$ ).  $z$  is measured in units of  $a_z^{-1}$  with  $a_z = 23107$  a.u.. In addition, a dark solid line shows the fermionic density  $n_0^{F,z}(z)$  [Eq. (10)], and a grey solid line the square of the trial wave function component in the  $z$  direction [Eq. (11)]. The dashed line shows the density profile for the Tonks limit [Eq. (12)].

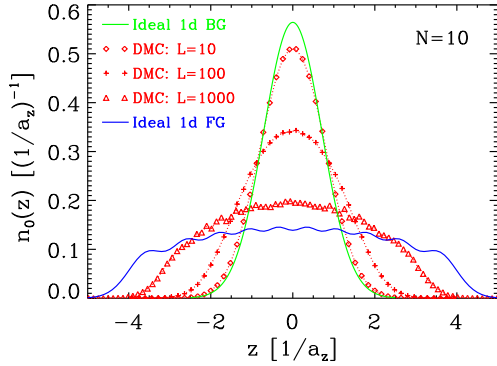


FIG. 7. DMC density  $n_0^{DMC,z}$  for  $N = 10$  as a function of  $z$  for four different aspect ratios,  $L = 10$  (diamonds), 100 (crosses), and 1000 (triangles).  $z$  is measured in units of  $a_z^{-1}$ , where  $a_z = 23107$  a.u.. In addition, a grey solid line shows the ideal gas density for bosons [Eq. (9)], and a dark solid line shows that for fermions [Eq. (10)]. The DMC density is close to  $n_0^{B,z}$  for small  $L$ , and approaches  $n_0^{F,z}$  as  $L$  increases.

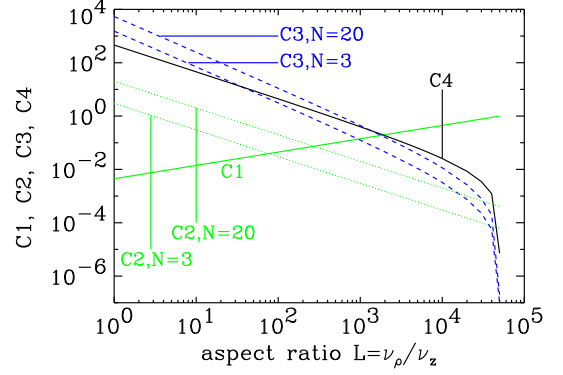


FIG. 8. Criteria  $C1$  (grey solid line),  $C2$  (grey dotted lines),  $C3$  (dark dashed lines), and  $C4$  (dark solid line) as a function of the aspect ratio  $L$  on a log-log scale using  $a = 100$  a.u.,  $m = m(^{87}\text{Rb})$  and  $\nu_z = 77.78$  Hz (see Sec. III C).  $C1$  and  $C4$  are independent of  $N$ , while  $C2$  and  $C3$  scale with  $N$  and  $N^{2/3}$ , respectively.  $C2$  and  $C3$  are shown for  $N = 3$  and  $N = 20$ .

| $L$    | $a_\rho$ [a.u.] | $a_{1d}$ [a.u.]       |
|--------|-----------------|-----------------------|
| 1.     | 23107.          | $-5.3 \times 10^6$    |
| 5.     | 10328.          | $-1.1 \times 10^6$    |
| 10.    | 7307.           | $-5.3 \times 10^5$    |
| 50.    | 3268.           | $-1.0 \times 10^5$    |
| 100.   | 2311.           | $-5.1 \times 10^4$    |
| 500.   | 1033.           | $-9.6 \times 10^3$    |
| 1000.  | 731.            | $-4.6 \times 10^3$    |
| 5000.  | 327.            | $-7.3 \times 10^2$    |
| 10000. | 231.            | $-3.0 \times 10^2$    |
| 50000. | 103.            | $-8.3 \times 10^{-2}$ |

TABLE I. Characteristic length  $a_\rho$  and one-dimensional scattering length  $a_{1d}$  for  $a = 100$  a.u.,  $m = m(^{87}\text{Rb})$ ,  $\nu_z = 77.78$  Hz, and  $a_z = 23107$  a.u. as a function of the aspect ratio  $L$ .